PAPER

Fabrication of Ti substrate grain dependent C/TiO2 composites through carbothermal treatment of anodic TiO2†

Celine Rüdiger,‡*[ab] Marco Favaro,§[c] Carlos Valero-Vidal,¶[b] Laura Calvillo,[c] Nathalie Bozzolo,[d] Suzanne Jacomet,[d] Clivia Hejny,[e] Luca Gregoratti,[f] Matteo Amati,[f] Stefano Agnoli,[c] Gaetano Granozzi[c] and Julia Kunze-Liebhäuser*[b]

Composite materials of titania and graphitic carbon, and their optimized synthesis are highly interesting for application in sustainable energy conversion and storage. We report on planar C/TiO2 composite films that are prepared on a polycrystalline titanium substrate by carbothermal treatment of compact anodic TiO2 with acetylene. This thin film material allows for the study of functional properties of C/TiO2 as a function of chemical composition and structure. The chemical and structural properties of the composite on top of individual Ti substrate grains are examined by scanning photoelectron microscopy and micro-Raman spectroscopy. Through comparison of these data with electron backscatter diffraction, it is found that the amount of generated carbon and the grade of anodic film crystallinity correlate with the crystallographic orientation of the Ti substrate grains. On top of Ti grains with ~(0001) orientations the anodic TiO2 exhibits the highest grade of crystallinity, and the composite contains the highest fraction of graphitic carbon compared to Ti grains with other orientations. This indirect effect of the Ti substrate grain orientation yields new insights into the activity of TiO2 towards the decomposition of carbon precursors.

[a] *Physik-Department, Technische Universität München, James-Franck-Str. 1, 85748 Garching, Germany. E-mail: Celine.Ruediger@uibk.ac.at; Tel: +43 (0) 512 507 58018*

[b] *Institut für Physikalische Chemie, Leopold-Franzens-Universität Innsbruck, Innrain 52c, 6020 Innsbruck, Austria. E-mail: Julia.Kunze@uibk.ac.at; Tel: +43 (0) 512 507 58013*

[c] *Dipartimento di Scienze Chimiche, Università di Padova, Via Marzolo 1, 35131 Padova, Italy*

[d] *MINES ParisTech, PSL – Research University, CEMEF – Centre de Mise en Forme des Matériaux, CNRS UMR 7635, CS 10207 Rue Claude Daunesse, 06904 Sophia Antipolis Cedex, France*

[e] *Institut für Mineralogie und Petrographie, Leopold-Franzens-Universität Innsbruck, Innrain 52d, 6020 Innsbruck, Austria*

[f] *Elettra – Sincrotrone Trieste SCpA, SS14-Km163.5 in Area Science Park, 34149 Trieste, Italy*

† Electronic supplementary information (ESI) available: Additional details on experimental methods. Optical appearance of TiO2^{ref} and C/TiO2. Additional Raman measurements of TiO2^{ref} and C/TiO2, evaluation of Raman spectra, and additional Raman analysis. Raman spectra of oriented anatase single crystals. SPEM results of a reference sample with TiC/TiO species. Roughness analysis of TiO2^{ref} by AFM. See DOI: 10.1039/c5cp07727c

‡ Present address: Institut für Physikalische Chemie, Leopold-Franzens-Universität Innsbruck, Innrain 52c, 6020 Innsbruck, Austria.

§ Present address: Advanced Light Source (ALS) and Joint Center for Artificial Photosynthesis (JCAP), Lawrence Berkeley National Laboratory, 1 Cyclotron Rd., Berkeley, CA 94720, USA.

¶ Present address: Advanced Light Source (ALS) and Joint Center for Energy Storage Research (JCESR), Lawrence Berkeley National Laboratory, 1 Cyclotron Rd., Berkeley, CA 94720, USA.

1. Introduction

Composite materials of titania and conductive graphitic carbon have gained particular research interest for application in photocatalysis, dye sensitized solar cells (DSSCs), Li-ion batteries and proton exchange membrane fuel cells (PEMFCs) due to the enhanced performance of the composite compared to TiO2 or C alone.[1–5] It was shown that the application-specific performance of C/TiO2 hybrid materials is highly sensitive to the synthesis route[6] and the detailed preparation conditions.[1,7,8] There is evidence that the major benefits of functional C/TiO2 nanocomposites, such as their superior stability and electric conductivity, rely on a close contact between conductive carbon and TiO2.[9,10] Hence, an adapted synthesis is of vital importance to optimize application-specific functional properties.

Biphasic C/TiO2 or mixed TiO$_x$C$_y$ (rich in TiC/TiO) materials with different morphologies, such as nanotubes, nanoparticles or thin films, can be prepared *via* carbothermal treatment of initially prepared titania precursors with reactive acetylene (C2H2) in a gas flow reactor.[11–15] These materials have been tested as catalyst supports in studies of the electrochemical reduction of oxygen[11] or oxidation of small alcohols,[12,16,17] and as Li-ion battery anodes,[15] and exhibited promising performances. The employed carbothermal route provides realistic process conditions that are relevant for the production of high surface area

This journal is © the Owner Societies 2016

functional materials based on TiO$_2$ and C. The physico-chemical properties of the thus prepared materials are empirically tailored *via* the synthesis parameters. An adapted design of functional composites requires a detailed understanding of the correlation between the synthesis conditions and the intrinsic physico-chemical properties of the produced materials.

In this context, planar anodic titania films that are carbothermally treated under reproducible conditions can be used to systematically study the synthesis–property–performance relationships, which are essential to identify the optimal synthesis procedure to obtain specific functional materials *via* the carbothermal route. Anodic films are particularly interesting due to their tunable morphology, which can be varied from compact films[18] to high aspect ratio self-organized nanotubes.[19] Several studies have been performed on carbothermally reduced compact anodic TiO$_2$, rich in TiO and TiC phases, to correlate the synthesis conditions with intrinsic physico-chemical properties, such as structure and composition, and with functional performance, such as (electro-)chemical stability or electrical conductivity.[14,16,17,20]

In a previous study, we have shown that the synthesis conditions of TiO$_x$C$_y$ films[14] significantly influence the catalytic activity of thereon deposited Pt nanoparticles towards the electro-oxidation of ethanol. Interestingly, it was found that the electrochemical stability of Pt/TiO$_x$C$_y$ appeared to be affected by the grain orientations of the polycrystalline Ti substrate.[16] This indicates that the texture of the Ti substrate, on which the precursor anodic film is prepared, constitutes an additional parameter that has to be taken into account when optimizing the synthesis of TiO$_x$C$_y$ films.

In view of the importance of C/TiO$_2$ composites for applications in energy conversion and storage, we present a study on the preparation of a thin carbon film on compact anodic TiO$_2$

on polycrystalline Ti (C/TiO$_2$/Ti$_{poly}$) by means of carbothermal treatment with C$_2$H$_2$ in a flow reactor at 550 °C. A special focus is given to the investigation of the substrate grain dependent physico-chemical properties of the C/TiO$_2$ composite film.

The films are *ex situ* characterized by means of local analysis tools. Electron backscatter diffraction (EBSD), micro-Raman spectroscopy, scanning electron microscopy (SEM), atomic force microscopy (AFM) and scanning photoelectron microscopy (SPEM) are used to correlate grain orientations of the polycrystalline Ti substrate with the local crystalline phase composition, surface topography and chemical composition of the C/TiO$_2$ films.

The present study sheds light on the origin of the substrate grain effect in carburized TiO$_2$/Ti$_{poly}$ systems and thereby shows the significance of the TiO$_2$ precursor properties for the synthesis of optimized functional C/TiO$_2$ composites *via* the carbothermal route.

2. Experimental section

Disks of 1 mm thickness and diameters of 10–15 mm were cut from a 20 mm diameter polycrystalline Ti rod (99.6% purity, temper annealed, Advent Ltd, England). One side of the sample was mechanically and electrochemically polished, following the procedure described in ref. 14 (see the detailed description in the ESI†). To enable the retrieval of identical spots on the samples, a cross-scratch was placed as a marker in the center of the electropolished area by using a tungsten needle.

The crystallographic texture of the electropolished Ti substrate was mapped by EBSD (see Fig. 1) using a FEI XL30 scanning electron microscope (SEM) operated at 20 kV accelerating voltage and equipped with a TSL-EDAX EBSD system. The step size of the EBSD map was set to 2 µm, which led to a suitable spatial resolution of the microstructure.
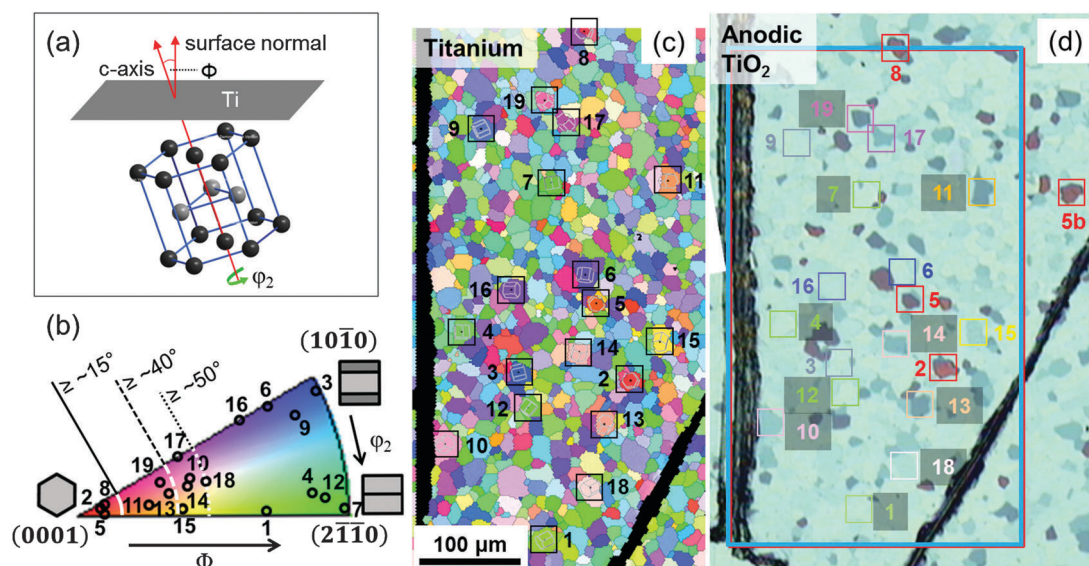

Fig. 1 (a) Schematic sketch of the orientation of the hexagonal lattice of Ti with respect to the Ti substrate surface. (b) Standard triangle of the surface-normal projected inverse pole figure orientation map (EBSD map) with numbers of the studied grains, ranges of tilt-angles Φ and the surface projected hexagonal cells. (c) EBSD map of a Ti substrate; (d) optical micrograph of the surface area shown in (c) after anodization.

This journal is © the Owner Societies 2016

Phys. Chem. Chem. Phys., 2016, **18**, 9220–9231 | 9221

The electropolished Ti samples were consecutively cleaned in an ultrasonic bath with ethanol (technical grade), isopropanol (high purity) and de-ionized (DI) water (Millipore-Milli-Q system, 18.2 MΩ). Compact amorphous TiO_2 films were produced by potentiostatic electrochemical anodization in a home-built Teflon electrochemical cell with a two-electrode configuration using a DC power supply controlled by a multimeter, and applying the following settings: anodization at 20 V for 600 s in 0.1 M sulfuric acid (H_2SO_4, analytical grade, 95–97%, Merck, Germany) electrolyte at room temperature using a platinum mesh counter electrode.[14] The anodic films were rinsed with DI water and dried in an argon (Ar 4.8, Linde, Germany) stream.

A carbon layer was synthesized on the anodic film by carbothermal treatment in a tubular quartz reactor under controlled gas flow. The gas flow and acetylene dose were optimized for the reactor geometry. In a reactor tube of 40 mm diameter, the following procedure was applied: [i] purged for two hours under a high flow of Ar to remove air, [ii] heated for up to 90 min at a constant rate to 550 °C in 200 standard cubic centimeters per minute (sccm) Ar, [iii] maintained for 60 min at 550 °C, [iv] 0.5 flow% of acetylene (C_2H_2, solvent-free, Linde, Germany) was added for 5 min, [v] maintained for 60 min at 550 °C in Ar, and [vi] the oven was left to cool down to room temperature. These samples will be referred to as C/TiO_2. A reference sample (termed TiO_2^{ref}) was thermally treated in 200 sccm Ar without C_2H_2 according to the sequence [i]–[ii]–[v]–[vi].

After anodization and thermal treatment, optical micrographs were acquired for the reference sample using a camera of 10× magnification (belonging to the AFM equipment). The surface morphology of TiO_2 and C/TiO_2 was investigated using a field emission SEM based on a GEMINI column in a Zeiss CrossBeam NVision 40 system. Micrographs were acquired with the in-lens secondary electron detector using an acceleration voltage of 4 kV and working distances of 4–7 mm. AFM was performed as described in the ESI.†

Micro-Raman spectroscopy was applied to investigate the crystalline phase composition of C/TiO_2 and TiO_2^{ref}. A Jobin Yvon Horiba HR800 instrument equipped with a Nd:YAG laser (532 nm) was used in a non-focal operation mode and without a polarizer to analyze the average chemical composition and structure of the film on top of individual Ti substrate grains. The size of the focused laser spot on the sample was about 5 μm using the 50× magnification of the optical microscope. Backscattered Raman signals were recorded with a resolution of less than 2 cm^{-1} (as determined by measuring the Rayleigh line) in a spectral range from 80 to 2000 cm^{-1}.

SPEM was performed at the ESCAmicroscopy beamline at the Elettra Synchrotron Facility in Trieste, where the X-ray photon beam was demagnified by a Zone Plate to a sub-micron spot of about 150 nm onto the sample, which was then rastered to produce an image by detecting the photoelectrons generated from the sample.[21] In this work the photon energy was set to 756 eV. The incident X-ray beam was normal to the sample surface while the angle between the hemispherical electron analyzer (HEA) and the sample surface was 30°. Photoelectron maps of 50×50 μm^2 were recorded by sampling the surface with a step of 0.2 μm and a dwelling time of 60 ms per pixel. The HEA was equipped with a multichannel electron detector which simultaneously acquires 48 maps (channels), each tuned to a specific photoelectron energy within a selected energy window. This allowed the (i) extraction of spectra from a selected area of the acquired photoelectron micrograph with an energy window of 7.8 eV and a step of 0.164 eV and (ii) removal of the topographic contributions to the photoelectron micrographs and extraction of the chemical contrast. The chemical contrast micrographs (chemical maps) were obtained by selecting, from the recorded 48 maps, those acquired at the photoelectron peak energy and those acquired at an energy related to the background of the photoelectron peak, integrating them to obtain two maps corresponding to the photoelectron peak and background intensity, and determining their ratio.[22] The ratio of photoelectron maps acquired in the spectral regions of the C 1s and Ti 2p core levels with their corresponding background is referred to as C/BG and TiO_2/BG, respectively. For elemental analysis of the C/TiO_2 composite, the uncorrected absolute peak area was used as a qualitative measure, which was obtained from integration of the spectra from the image after subtraction of a constant background.

Additional information about the performed experiments can be found in the ESI.†

3. Results

3.1 Identification of substrate grain orientations

The crystallographic orientations of the Ti substrate grains are determined by EBSD, which provides the three Euler angles, φ_1, Φ and φ_2, which define the crystallographic orientation of the hexagonal unit cell with respect to the substrate surface (according to the Bunge convention[23]). The sketch in Fig. 1 illustrates the orientation of the hexagonal lattice[24] with respect to the substrate surface: Φ gives the tilt angle of the unit cell c-axis with respect to the surface normal and φ_2 gives the azimuthal rotation of the hexagonal unit cell around its c-axis.[23,25] A rotation of the Ti substrate around its surface normal is described by the angle φ_1 (not shown in Fig. 1). The two Euler angles Φ and φ_2 can be restricted to $0° \leq \Phi \leq 90°$ and $0° \leq \varphi_2 \leq 30°$ due to the symmetry of the hexagonal lattice. For the azimuthal rotation the zero point is chosen to coincide with the $(10\bar{1}0)$ plane for $\Phi = 90°$, while $\varphi_2 = 30°$ and $\Phi = 90°$ yield the $(2\bar{1}\bar{1}0)$ plane. The crystallographic orientation of individual substrate grains can be illustrated in a surface-normal projected inverse pole figure orientation map (from now on termed EBSD map) like in Fig. 1c that uses an RGB color code defined in the standard triangle in Fig. 1b. From the colors in the standard triangle the crystallographic direction parallel to the sample surface normal can be deduced.

EBSD and optical microscopy are used to generate a correlation map between the Ti substrate grain orientation and the optical appearance of the anodic oxide film. Fig. 1 shows the EBSD map of an electropolished titanium substrate and an optical micrograph of the same surface after anodization. According to

9222 | *Phys. Chem. Chem. Phys.*, 2016, **18**, 9220–9231

This journal is © the Owner Societies 2016

ellipsometry measurements (not shown), the fresh anodic TiO_2 film has an average thickness of ~ 53 nm. The comparison of Fig. 1c and d reveals that the interference colors of the anodic TiO_2 are strongly affected by the orientation of the Ti substrate grains. In particular, the substrate tilt angle Φ has an important impact on the optical properties of the oxide film. Variations in interference properties are directly related to variations in the TiO_2 film thickness. Under the applied synthesis conditions, dark colors correspond to thinner films, and bright colors to thicker TiO_2 films.[26,27] We can define four ranges of substrate tilt angles Φ that cause different interference colors of the oxide film (see Fig. 1b). The azimuthal substrate orientation, described by φ_2, has only a minor effect on the interference colors of the anodic film (see ESI†). Due to the rotational symmetry of the oxide film thickness on individual grains, the corresponding orientation angle φ_1 does not affect the interference color of the anodic TiO_2. Table 1 summarizes the assignment of the oxide colors to the tilt angles Φ of the Ti substrate. This allows an estimation of the substrate orientations without the necessity of an EBSD measurement. The two orientations $\sim Ti\{10\bar{1}0\}$ ($\varphi_2 \sim 0°$) and $\sim Ti\{2\bar{1}\bar{1}0\}$ ($\varphi_2 \sim 30°$) can be deduced

(without EBSD map) from the optical appearance of the anodic film after thermal treatment at 550 °C (see Fig. S1 and the discussion in ESI†).

In the following, we will focus on the relationship of local chemical and physical properties, obtained by microscopic and spectroscopic techniques of planar $C/TiO_2/Ti_{poly}$ composite materials, and the tilt angle Φ of the Ti substrate grains. The restriction to Φ is motivated by studies of the TiO_2/Ti_{poly} system reported in the literature, which suggest that variations of the tilt angle Φ have a stronger influence on many physical and chemical properties of anodic TiO_2 than the c-azimuthal orientation (given by φ_2).[25,28,29]

3.2 Thermal treatment with C_2H_2

Fig. 2 shows top-view scanning electron micrographs of the as-grown anodic TiO_2 and the C/TiO_2 composite film in the same surface area. On both films, the grain boundaries of the underlying Ti substrate are clearly visible. The crystallographic orientations of the substrate grains are indicated by surface projected hexagonal cells. The morphology of the anodic film varies for differently oriented substrate grains (Fig. 2b), which is a

Table 1 Assignment of crystallographic Ti substrate orientations to anodic TiO_2 film colors

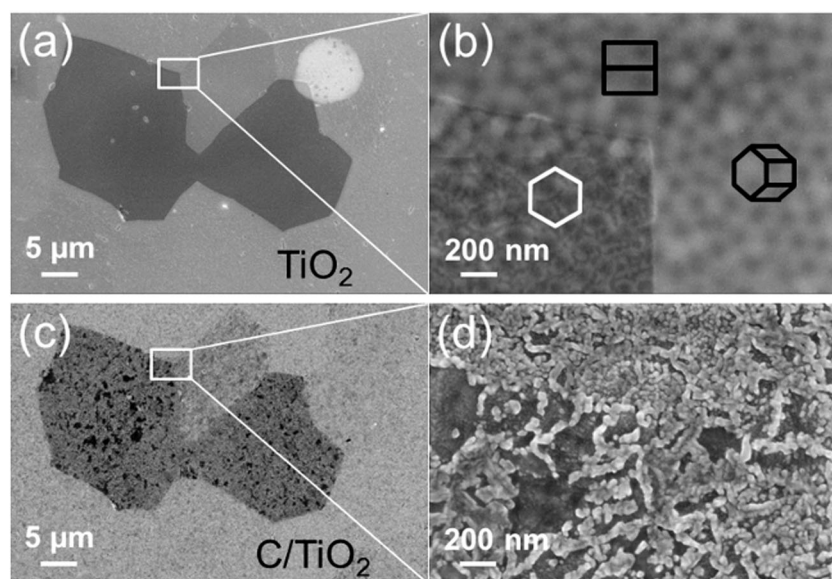| Interference color (thickness) of TiO_2	Dark red (thin TiO_2)	Dark violet/blue	Blue	Bright blue (thick TiO_2)	
Tilt angle Φ of Ti	$0° \leq \Phi \leq \sim 15°$	$\sim 15° \leq \Phi \leq \sim 40°$	$\sim 40° \leq \Phi \leq \sim 50°$	$\Phi \geq \sim 50°$ (*i.e.* all $\sim Ti\{hki0\}$)	
Ti($hkil$)[a]	$\sim Ti(0001)$			$\sim Ti\{10\bar{1}0\}$	$\sim Ti\{2\bar{1}\bar{1}0\}$
EBSD map colors	Red	Pink-orange	Purple-yellow	Blue	Green
Representative hexagonal cell	⬡	⬡	⬡	▭	▭

[a] See also ESI.

Fig. 2 Scanning electron micrographs of a selected area on the anodic TiO_2 film (a and b) and of the same area on the C/TiO_2 film (c and d), with hexagonal cells representing the Ti substrate grain orientations.

This journal is © the Owner Societies 2016

Phys. Chem. Chem. Phys., 2016, **18**, 9220–9231 | 9223

well-studied phenomenon.[29] After the carbothermal treatment at 550 °C, a granular film has formed on top of the anodic film (Fig. 2d). The morphology and the coverage of the deposit seem to be different on different substrate grains.

The crystalline phases and the chemical composition of the C/TiO$_2$/Ti$_{poly}$ composite are determined using micro-Raman spectroscopy. The average Raman response of the film on top of single substrate grains is measured, since the focused laser beam has a lateral size of $\sim$5 μm, whereas the grains have a size of 10–20 μm. In the present case, the penetration depth is much larger than the C/TiO$_2$ film thickness (see discussion in the ESI†), therefore the Raman signal originates from the entire composite film. Fig. 3 shows micro-Raman spectra of C/TiO$_2$ for three ranges of Ti substrate tilt angles Φ. To exclude contributions of carbon contamination from secondary sources, no EBSD map was obtained for the electropolished Ti surface of this sample. All six bands of first order Raman scattering of anatase TiO$_2$ are detected between 100 and 830 cm^{-1} in the C/TiO$_2$ film.[30] Due to the high proximity of the A$_{1g}$ band and the high frequency B$_{1g}$ band, they appear as one peak at $\sim$517 cm^{-1}. The weak shoulders at 320 cm^{-1} and 695 cm^{-1} can be attributed to combination bands of the anatase spectrum due to second-order Raman scattering.[30] The two most intense peaks of rutile, E$_g$ and A$_{1g}$, are present, as well as its most prominent combination band at $\sim$235 cm^{-1}.[31] Peaks found at $\sim$267 cm^{-1} and

$\sim$347 cm^{-1} can be attributed to the most intense Raman signals of Ti$_2$O$_3$.[32,33] The broad features between $\sim$240 and $\sim$395 cm^{-1} cannot be clearly identified. The Raman spectra reveal that the anodic TiO$_2$ contains crystalline domains of anatase and rutile and is partially reduced after the carbothermal treatment with C$_2$H$_2$.

The spectra detected for different ranges of Φ clearly show that the phase composition of the film is affected by the underlying Ti substrate grain orientations. The fractions of crystalline anatase and rutile phases in the film can be deduced from the relative intensities of the corresponding Raman bands.[34] A comparison between the most intense anatase B$_{1g}$ band ($\sim$399 cm^{-1}) and the rutile E$_g$ band ($\sim$447 cm^{-1}), and between the rutile A$_{1g}$ band ($\sim$612 cm^{-1}) and the high frequency anatase E$_g$ band ($\sim$639 cm^{-1}) indicate that there is considerably more rutile present in the thermally treated anodic TiO$_2$ film on top of grains with $\Phi \leq \sim$15° than in the film on top of grains with $\Phi \geq \sim$50°. Grains with $\sim$15° $\leq \Phi \leq \sim$50° exhibit mixed phase compositions.

All spectra depicted in Fig. 3 show two strong broad peaks at $\sim$1348 and $\sim$1600 cm^{-1} that are the characteristic D- and G-bands of carbon and can be attributed to nanocrystalline graphite (NCG).[35] The ratio of the D-band intensity to the G-band intensity is determined by means of a 4-peak Gaussian fit and yields values of 0.7–0.8 independent of the substrate grain orientations (see Fig. S2 in the ESI†), which correspond to NCG clusters of approximately 6 nm diameter according to the Tuinstra–Koenig relation.[35]

The carbon signal intensity appears to be influenced by the substrate grain orientation. In Fig. 3 the integrated and normalized areas of the Raman signals that correspond to vibrations of carbon, I(C), are plotted versus the tilt angles Φ of the Ti substrate grains. I(C) decreases markedly with increasing substrate tilt angle; on top of substrate grains with $\Phi \leq \sim$15°, the intensity is about 2 times higher than on top of substrate grains with tilt angles $\Phi \geq \sim$50°. The Raman response of the C/TiO$_2$ composite film differs considerably from the spectrum of a reference sample (TiO$_2^{ref}$) that underwent the same thermal treatment without the addition of C$_2$H$_2$ (see Fig. 3). The intensities of the carbon bands detected on TiO$_2^{ref}$ are much lower than the ones detected on the C/TiO$_2$ composite, which evidences that the high amount of carbon in the latter originates from the decomposition of C$_2$H$_2$ and not from carbon contamination.

SPEM is performed on the C/TiO$_2$ composite to gain complementary information about the local chemical surface composition and its dependency on the Ti substrate grain orientation. The corresponding results are summarized in Fig. 4. Cross-correlation with EBSD allows for the assignment of crystallographic orientations to the Ti substrate grains underneath the anodic TiO$_2$ film. It is important to note that only the region at the left of the dashed line in Fig. 4b coincides with the EBSD map that was acquired on the Ti substrate, which enables the identification of possible carbon contamination generated during the EBSD measurement. The grain labeled A in Fig. 4 belongs to substrate orientations with 0° $\leq \Phi \leq \sim$15°, whereas the grains labelled B and C are
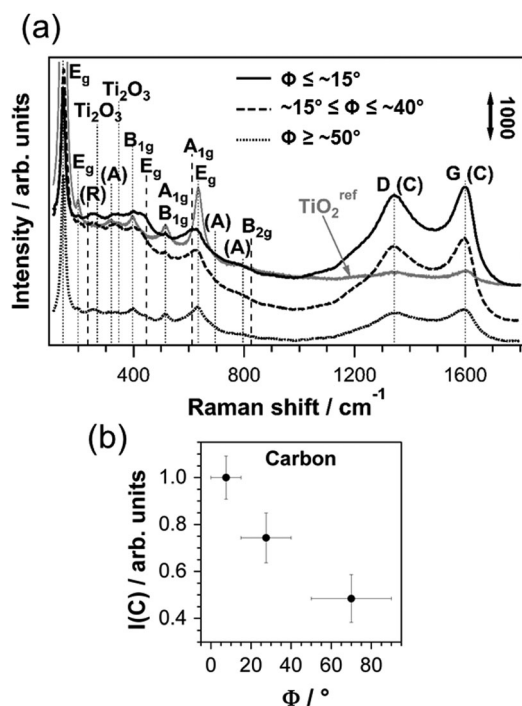

Fig. 3 (a) Micro-Raman spectra of C/TiO$_2$ on Ti$_{poly}$ for different ranges of tilt angles Φ. For clarity, the spectra are shifted vertically. TiO$_2^{ref}$: the spectrum of the anodic TiO$_2$ film on Ti with $\Phi \leq \sim$15° after thermal treatment without C$_2$H$_2$. Dashed lines: rutile bands, dotted lines: all other bands. D- and G-bands: from carbon (C). TiO$_2$ combination bands: (R) = rutile, (A) = anatase. (b) Integrated peak areas of carbon bands versus Φ. Error bars of I(C): standard deviations of I(C) on grains within one Φ-range; error bars of Φ: ranges defined in Table 1.
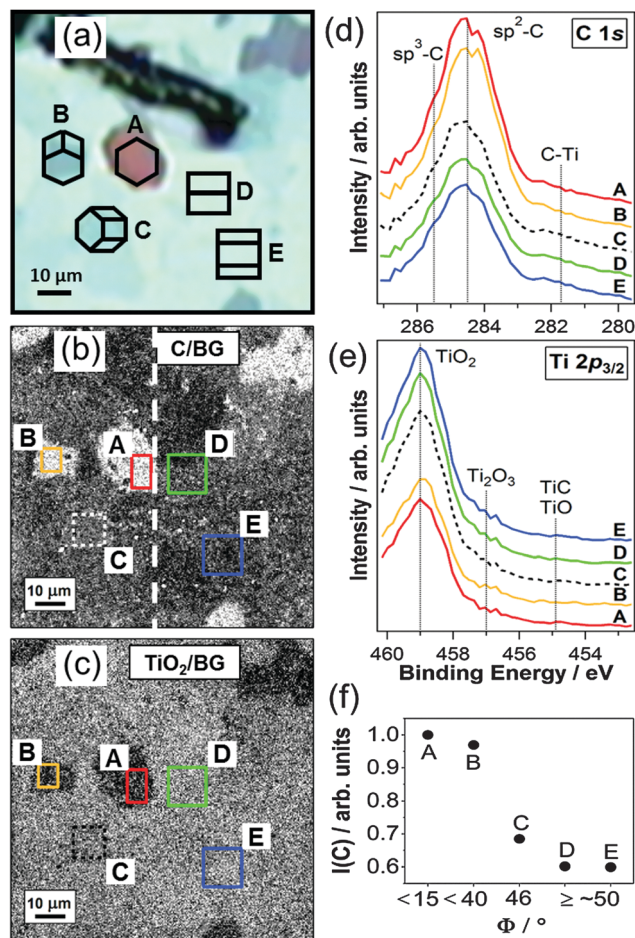
Fig. 4 (a) Optical micrograph of the anodic TiO_2 film with surface projected hexagonal cells representing Ti substrate grain orientations (A–E). Chemical maps of the C 1s (b) and Ti $2p_{3/2}$ (c) core levels obtained for the same film by SPEM after thermal treatment with C_2H_2 at 550 °C. Spectra extracted from the boxes in the C 1s (d) and the Ti $2p_{3/2}$ (e) chemical maps. For clarity, the spectra are shifted vertically. (f) Integrated C 1s signal intensities, derived from (d), versus tilt angle Φ of Ti substrate grains.

characterized by underlying substrate tilt angles of $\sim 15° \leq \Phi \leq \sim 40°$ and $\sim 40° \leq \Phi \leq \sim 50°$, respectively. Grains D and E correspond to substrate orientations with $\Phi \geq \sim 50°$ (see hexagonal cells in Fig. 4a). From Fig. 4 it can be seen that the chemical composition of the carbothermally treated film surface is considerably affected by the properties of the Ti substrate grains. In the chemical map of Fig. 4b brighter contrast corresponds to a relatively higher C 1s signal, evidencing an accordingly higher amount of carbon. In the same areas, the contrast in Fig. 4c appears darker. This can be explained by the presence of a thicker carbon layer on top of the anodic TiO_2 film that attenuates the intensity of the Ti 2p core level photoelectrons. Interestingly, the film on grain C, whose underlying Ti substrate is tilted by $\Phi = 46°$, appears to be just at the transition from high to low carbon content, since it is barely distinguishable from the surrounding area of the homogeneous shade in the chemical maps. No change in contrast can be observed across the dashed line in Fig. 4b, which proves the absence of artefacts caused by the acquisition of the EBSD map. Fig. 4d and e report the C 1s

and Ti $2p_{3/2}$ spectra extracted from the indicated areas of the photoelectron micrographs. The C 1s peaks of all the studied grains are clearly dominated by the signal of graphitic carbon (sp^2 hybridized carbon), detected at 284.5 eV.[36] This is in accordance with the Raman response of the C/TiO_2 composite, which proves the presence of NCG. The weak shoulder occurring at 285.6 eV accounts for a small fraction of diamond-like carbon (DLC, sp^3 hybridized carbon).[20,36] No defined peak of carbidic carbon (C–Ti bonds) is found at 281.7 eV (see Fig. S3 in the ESI†), hence only a negligible amount of this species is present at the C/TiO_2 interface. For all studied grains, the Ti $2p_{3/2}$ region is dominated by the TiO_2 peak at 459 eV[20] that originates from the anodic film. The small shoulder at the low binding energy tail of the peak reveals the presence of reduced titania species, such as Ti(III) in Ti_2O_3 at 457 eV,[20] which confirms the Raman results. In accordance with the C 1s spectrum, no pronounced TiC (or TiO) component is detected at 454.9 eV in the Ti 2p spectrum (see Fig. S3 in ESI†). Fig. 4f shows the variation of the integrated and normalized carbon signal intensities $I(C)$, extracted from the C 1s photoelectron micrograph, with substrate grain orientation, which gives an estimate of the differences in carbon content. As already indicated by the contrast in the chemical maps, there is an abrupt drop in the carbon intensity from grains with small tilt angles Φ (A, B) to grains with high tilt angles Φ (D, E) and a transition between these two types of substrate grains represented by grain C. The carbon signal intensity of grain A is about 1.7 times higher than the one of grain D. This trend is consistent with the Raman results (Fig. 3b). The complementary contrast in the chemical maps confirms a layered structure of the C/TiO_2 composite with a carbon film on top of the anodic TiO_2.

In contrast, carbothermal treatment of anodic TiO_2 films carried out in UHV and with different carbon precursors are reported to yield a conversion to TiO and TiC after shorter annealing times and lower temperatures.[20,36] However, such TiO_xC_y compact films were found to suffer from partial re-oxidation to TiO_2 accompanied by the formation of graphitic carbon at the surface when exposed to ambient air. This was rationalized by DFT calculations which revealed that an increasing oxygen partial pressure favors the phase separation into graphitic carbon on top of anatase TiO_2.[20] In the present study, the anodic films are treated with acetylene in a flow reactor with the supporting gas argon, which involves higher oxygen partial pressures than under UHV conditions. Thus it is likely that these conditions hinder the formation of TiO_xC_y at 550 °C in favor of effective deposition of a carbon layer, or that only a low fraction of TiC and TiO species forms, which are easily re-oxidized upon exposure to air.

Since SPEM yields a photoelectron signal of TiO_2 on all substrate grains, the maximum carbon layer thickness can be estimated from the probing depth for atomically planar graphitic carbon, which yields a thickness of about 2.3 nm. A close look at the chemical maps reveals that the film on top of individual substrate grains has no perfectly homogeneous composition (see black spots on grain A in Fig. 4b), which is supported by the inhomogeneous coverage of the deposited

film that is observed by SEM (Fig. 2d). This finding is most likely related to the properties of the anodic TiO_2 at the moment that C_2H_2 interacts with it during the carbothermal treatment, which is described in the next section.

3.3 Thermal treatment without C_2H_2

During carbothermal treatment, C_2H_2 is added to the process after one hour of annealing at 550 °C under an argon gas flow. It can be expected that prior to the addition of C_2H_2, the properties of the anodic TiO_2 film, in particular its crystallinity, are different from those of the pristine film and that these properties affect the interaction with C_2H_2. Hence, the investigation of the substrate grain dependent properties of the anodic TiO_2 film prior to the addition of C_2H_2 may unravel the origin of the grain dependent chemical composition of the final $C/TiO_2/Ti_{poly}$ composite. For this purpose, a reference sample (TiO_2^{ref}) was prepared under the same conditions as the C/TiO_2 composite, but the annealing treatment was stopped prior to the introduction of C_2H_2. An EBSD map of the polycrystalline Ti substrate recorded after electropolishing allows a precise identification of the tilt angles Φ of the grains.

Fig. 5a shows the Raman response of the TiO_2^{ref} film on individual substrate grains that exhibit different tilt angles Φ. The colors of the spectra correspond to the substrate grain orientations that are indicated by black spots in the standard triangle (the studied grains are depicted in Fig. 1). Along the arrows, the tilt angle Φ of the substrate grains varies from 0° to 90°. In all spectra the characteristic bands of first-order Raman scattering of crystalline anatase TiO_2 are detected. The weak peaks at 320 cm^{-1} and 796 cm^{-1} are combination bands of anatase.[30] Apart from a weak feature around ~235 cm^{-1}, no distinct peaks in the spectrum can be attributed to rutile, which suggests a very low fraction of this phase in the TiO_2^{ref} film. All spectra show two peaks at ~1340 and ~1600 cm^{-1} that are the characteristic D- and G-bands of carbon, which indicate the presence of NGC.[35]

Fig. 5b shows the spectra of an anodic TiO_2 film on top of two different Ti substrate grains with $\Phi \geq \sim 50°$ (i.e. grains belonging to the group of $\sim Ti\{hki0\}$ orientations – see Table 1) and $\Phi \leq \sim 15°$ (i.e. $\sim Ti(0001)$). Apart from the weakly protruding E_g peak of anatase TiO_2 at 143 cm^{-1}, both Raman spectra are characterized by very broad and undefined features below ~ 1000 cm^{-1}, evidencing that the film is mainly amorphous.[37–39] The intensity of the Raman signal of the TiO_2 film on $\sim Ti(0001)$ is slightly higher than that of the film on $\sim Ti\{hki0\}$, which indicates that the grain orientation of the Ti substrate influences the properties of the pristine anodic TiO_2 film on top. The comparison between the Raman response of the TiO_2^{ref} system and the pristine anodic TiO_2 film discloses the changes that have occurred upon annealing: the thermal treatment at 550 °C leads to the crystallization of the anodic TiO_2 film. No graphitic carbon is detected on the pristine anodic TiO_2. The signal between 840 and 890 cm^{-1}, however, could be assigned to the Raman active C–C and C–O stretching of organic carbon contamination.[38–43] The carbon detected on TiO_2^{ref} may therefore originate from organic contamination adsorbed onto the surface of anodic
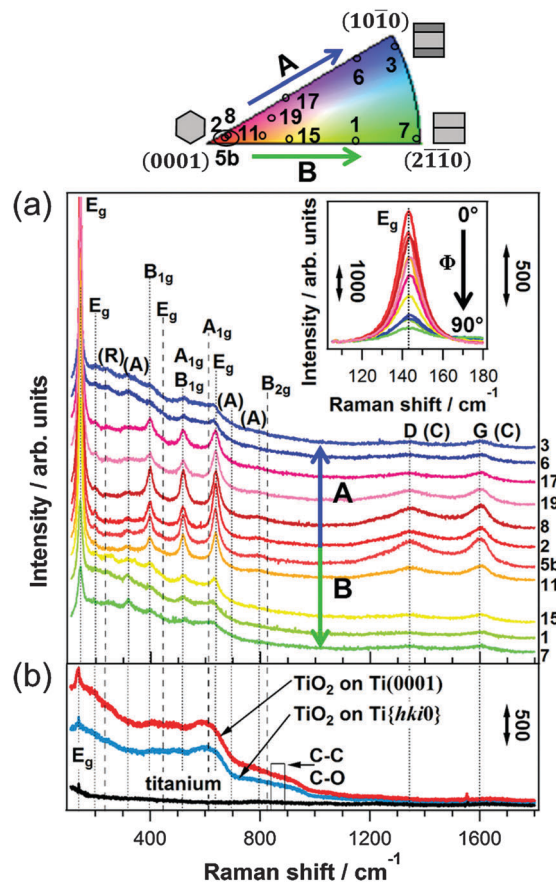

Fig. 5 (a) Micro-Raman spectra of TiO_2^{ref}. For clarity the spectra are shifted vertically. Dashed lines: rutile, dotted lines: anatase, carbon. D- and G-bands: carbon (C). TiO_2 combination bands: rutile (R), anatase (A). Inset: anatase E_g peak (143 cm^{-1}) evolution with tilt angle. Arrows (A and B): directions of Φ variation from 0° to 90°. (b) Micro-Raman spectrum of electropolished Ti (black) and an anodic TiO_2 film on $\sim Ti(0001)$ (red) and $\sim Ti\{hki0\}$ (blue).

TiO_2 and converted to graphitic carbon during the thermal treatment. An electropolished titanium substrate yields a flat baseline signal with almost no features (black spectrum in Fig. 5b). Only at around 143 cm^{-1} a small peak is detected which can be attributed to the corresponding E_g band of anatase TiO_2, arising most likely from the natural oxide film that is usually present on titanium. There is another small feature at about 1555 cm^{-1}, which might originate from carbon contamination as well and which is also present on the anodic TiO_2 film.

A strong influence of the substrate grain orientation on the Raman response of TiO_2^{ref} is found. While the anatase bands that are detected on top of grains with $\Phi \leq \sim 15°$ (red spectra in Fig. 5a) are relatively intense and sharp, the same peaks are not only weaker and broader when detected on grains with $\Phi \geq \sim 50°$ (green and blue spectra in Fig. 5a), but also embedded in a plateau-like background signal, which can be attributed to a considerable fraction of amorphous TiO_2 in these films. Well-defined, intense Raman bands of narrow full width at half maximum (FWHM) are characteristic of an extended single crystal (see Fig. S4 in the ESI†)[30,44] and are hence an indication of high crystallinity of the detected anatase phase. The more

intense the characteristic bands of anatase are, the higher is the fraction of this crystalline phase in the probed volume of TiO_2^{ref}. Peaks of small FWHM indicate a high long-range order and thus sufficiently large crystalline domains. The features of the amorphous TiO_2 background are also present, but less pronounced, on grains with intermediate tilt angles, $\sim 15° \leq \Phi \leq \sim 50°$ (orange, yellow, light and dark purple spectra in Fig. 4a), suggesting that the anodic TiO_2 film is partially crystalline on these grains. The crystallinity of the anatase phase gradually improves with decreasing Φ, as can be inferred from the evolution of the E_g band at 143 cm^{-1} (inset in Fig. 5a). A close comparison between the Raman spectra of grains 8, 2 and 5b (red in Fig. 5a) reveals a variation in relative peak heights of the three characteristic anatase bands detected between 350 and 650 cm^{-1}. This can be attributed to different preferential orientations of the anatase crystallites on these grains and is not related to varying crystallinity (see Fig. S4 and S5 and the discussion in the ESI†).

Together with the improvement of crystallinity in the TiO_2^{ref} film, an increase in the intensity of the characteristic D- and G-bands of NCG is observed with decreasing Φ. This suggests that the amount of produced graphitic carbon depends on the crystallinity of anodic TiO_2, and in particular on its anatase content.

For a detailed analysis of the dependency of the TiO_2 crystallinity and the carbon content on the substrate tilt angle, the low frequency E_g (~ 143 cm^{-1}), the B_{1g} (~ 396 cm^{-1}) and the high frequency E_g (~ 639 cm^{-1}) bands of anatase, as well as the Raman signal of carbon are fitted using Lorentzian and Gaussian line shapes (see Fig. S6 in the ESI†). The fractions of the

crystalline TiO_2, the overall (*i.e.* crystalline and amorphous) TiO_2 and the overall carbon phase in the film are then proportional to the integrated areas (*i.e.* intensities I) of the corresponding Raman signals (see ESI†). To eliminate the possible effects of surface roughness of the TiO_2^{ref} film on the quantity of generated NCG, the carbon signal intensities are corrected for the topographic surface area ($I_{spec}(C)$), which was determined by AFM (see Fig. S7 in the ESI†). The obtained results are reported in Fig. 6.

The overall fraction of crystalline anatase stays almost constant and low for $\Phi \geq \sim 50°$ and abruptly increases below $\Phi \sim 50°$ to five times higher values (Fig. 6a). The intensities of the B_{1g} (~ 396 cm^{-1}) and the high frequency E_g bands (~ 639 cm^{-1}) of anatase follow the same trends (see Fig. S8a in the ESI†). In addition, a progressive blue-shift of the B_{1g} band from ~ 397 to ~ 402 cm^{-1} and a parallel red-shift of the E_g band from ~ 637 to ~ 628 cm^{-1} are observed when the tilt angle Φ increases from 0° to 90°, which can be attributed to an increasing fraction of amorphous TiO_2 (see Fig. S8b and c in the ESI†).

The FWHM of the anatase E_g band (~ 143 cm^{-1}) drops linearly with decreasing Φ (Fig. 6b). For anatase TiO_2 nanocrystals, the FWHM of the E_g band was reported to be inversely related to their dimensions.[44–46] Hence, this trend indicates a continuous increase of the size of the crystalline anatase domains with decreasing Φ. However, the smallest FWHM value of about 12 cm^{-1} is still higher than the value of 7 cm^{-1} that is expected for bulk anatase TiO_2 (see Fig. S4 in the ESI†).[44,47] Therefore, the thermally treated anodic TiO_2 film can be considered polycrystalline on top of every single substrate grain. Similar FWHM values
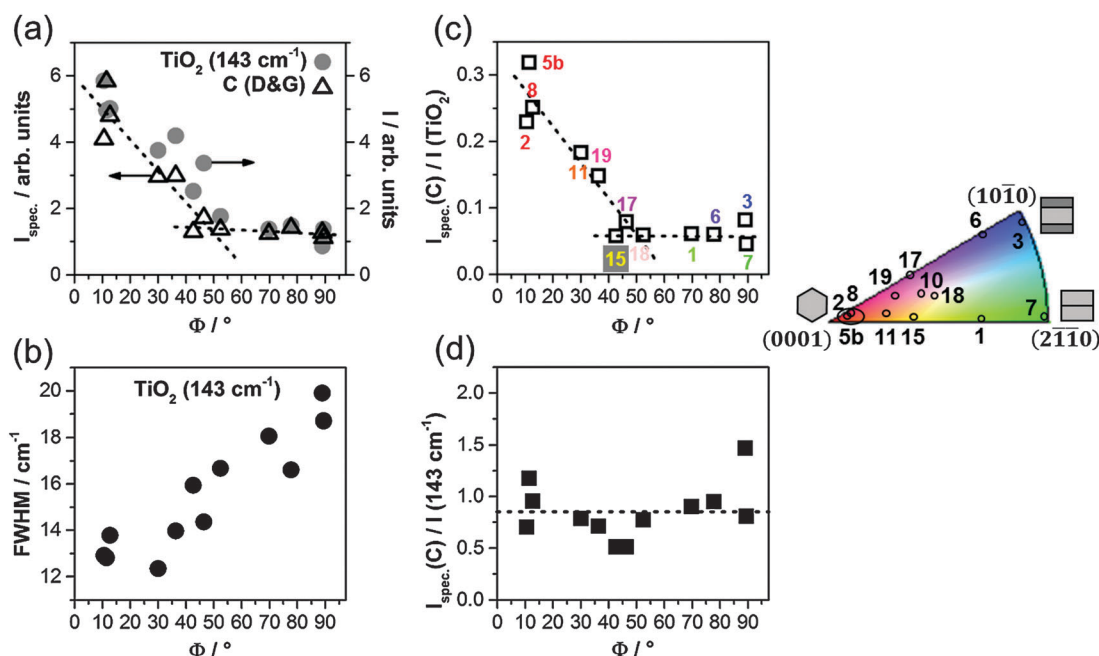

Fig. 6 Evaluation of Raman spectra of TiO_2^{ref} as a function of the substrate tilt angle Φ. The studied grains are labeled with numbers and marked in the standard triangle. (a) Anatase E_g band intensities at ~ 143 cm^{-1} and area-specific carbon signal intensities ($I_{spec}(C)$); (b) FWHM of the anatase E_g band at ~ 143 cm^{-1}. (c) The ratio of $I_{spec}(C)$ and the overall Raman response of crystalline and amorphous TiO_2 ($I(TiO_2)$). (d) The ratio of $I_{spec}(C)$ and the intensity of the anatase E_g band at ~ 143 cm^{-1}. Dashed lines in (a) and (c): linear least squares fits of carbon band intensities below 55° and above 40°. Dashed line in (d): arithmetic mean (0.85 ± 0.27).

This journal is © the Owner Societies 2016

Phys. Chem. Chem. Phys., 2016, **18**, 9220–9231 | 9227

were obtained for anatase TiO_2 nanoparticles with a crystallite size of less than $\sim$20 nm,[46] thus the domain sizes for thermally treated anodic TiO_2 are in the nanometer range.

The area-specific carbon signal intensities, $I_{spec}(C)$, give a qualitative measure of the amount of carbon on the thermally treated anodic film. From Fig. 6a it can be seen that $I_{spec}(C)$ follows the same trend with the substrate tilt angle as the intensity of the anatase E_g band. In Fig. 6c, $I_{spec}(C)$ is divided by the overall Raman response of TiO_2, $I(TiO_2)$, (including the amorphous phase) on individual substrate grains. As in Fig. 6a, two regions of different slopes can be identified and the crossing of the corresponding least squares linear fits (dashed lines) yields the tilt angle $\Phi \sim 50°$ as a threshold value. Below this point, $I_{spec}(C)/I(TiO_2)$ and therewith the amount of NCG that is produced on the TiO_2^{ref} upon thermal treatment is increased substantially. When $I_{spec}(C)$ is only divided by the intensity of the anatase E_g band (143 cm^{-1}), a plot versus Φ yields an almost constant line (Fig. 6d). This evidences that the two quantities, i.e. the amount of NCG and crystalline TiO_2, are closely linked. The intensity ratio of the carbon bands is determined to be 0.7–0.8, independent of the crystallographic orientations of the substrate grains underneath the film, which corresponds to NCG clusters of approximately 6 nm on the overall film (see ESI†).

4. Discussion

4.1 Crystallinity of the anodic film

The phase evolution of anodic titania films during isothermal annealing proceeds from initially amorphous TiO_2 to phase-pure anatase, over mixed phases of anatase and rutile towards phase pure rutile TiO_2, where the final phase composition depends on the annealing temperature, atmosphere and duration.[38,39,48] A variation of the tilt angle Φ of the substrate grains from $\sim$50° to 0° appears to have the same effect on the final crystallinity of TiO_2^{ref} as an enhancement of annealing temperature. This implies that the substrate grain orientation, and in particular the tilt angle Φ, has a strong impact on the kinetics of the phase transition. From the literature it is known that the compact anodic TiO_2 on top of $\sim$Ti(0001) is thinner than on $\sim$Ti{hki0} and contains higher donor concentrations, i.e. oxygen vacancies.[26,49,50] This is likely to affect the atomic reorganization or diffusion processes during annealing and therewith yield a higher isothermal crystallization rate for TiO_2 on $\sim$Ti(0001) than for TiO_2 on $\sim$Ti{hki0}. In particular, a considerable increase of donor density, supported by a parallel increase in the electron transfer rate, oxygen evolution current and photocurrent, has been found for anodic TiO_2 films on top of Ti substrate grains with tilt angles decreasing below $\Phi \sim 45°$,[25,28] which is in very good agreement with the observed increase of TiO_2 crystallinity for tilt angles $\Phi \leq \sim$50° (see Fig. 6a).

The difference in phase composition of TiO_2^{ref} and C/TiO_2 is related to the annealing time, which is longer for the thermal treatment with C_2H_2, hence yielding a considerable fraction of rutile TiO_2; in addition, the carbon present on the TiO_2 may have an effect on the crystallization kinetics.[51,52]

4.2 Carbon content in the C/TiO_2 composite

SPEM, micro-Raman spectroscopy and SEM evidence that carbothermal treatment of a compact anodic TiO_2 film with C_2H_2 at 550 °C yields a C/TiO_2 composite material, consisting of a few nm thick nanocrystalline graphitic carbon film on top of slightly reduced, polycrystalline TiO_2. On the reference sample TiO_2^{ref}, which is thermally treated without C_2H_2, a significantly less amount of carbon is detected, which originates from organic or hydrocarbon contamination of the anodic TiO_2 only.

The carbon signal intensity, extracted from SPEM and micro-Raman spectroscopy, follows a very similar trend with Φ for both TiO_2^{ref} and C/TiO_2. There are mainly two classes of grains: class one comprises substrate grains with tilt angles of $0° \leq \Phi \leq \sim$40° where a relatively high amount of carbon is deposited on the oxide film; class two covers all grains with tilt angles $\Phi \geq \sim$50° that exhibit a relatively low fraction of carbon after the carbothermal treatment of the anodic TiO_2. Grains with $\sim$40° $\leq \Phi \leq$ $\sim$50° belong to a transition zone, where an orientation of $\Phi \sim 50°$ can be identified as a threshold value.

The nature of the carbon film found on TiO_2^{ref} and C/TiO_2 is very similar, as evidenced by the resembling shapes of the Raman responses of carbon: the evaluation of the carbon bands' intensity ratios yields a NCG cluster size of approximately 6 nm, independent of the substrate grain orientation and the carbon source.

The formation of a grain-dependent carbon layer under the applied carbothermal treatment strongly suggests that C_2H_2 (and even organic contamination) is not thermally but catalytically decomposed at the surface of TiO_2.[53] Furthermore, the presented results evidence that crystalline TiO_2, in particular the anatase phase, is able to decompose C_2H_2, since only a small amount of carbon is found on TiO_2 that is mainly amorphous. It has been reported that Ti^{4+}–O^{2-} Lewis acid–base pairs on the surface of crystalline TiO_2 are the active centers for a heterolytic dissociation of C_2H_2 initiating self-assembly processes of acetylene to form polycyclic aromatic hydrocarbons at room temperature and graphitic carbon at sufficiently high temperatures (650 °C in ref. 53).[54,55] Anatase TiO_2 was found to be particularly efficient for the decomposition of acetylene, which is in line with our findings.

The crystallinity of compact anodic films on polycrystalline Ti substrates is affected by the Ti substrate grain orientations. This causes the observed grain dependent average chemical surface composition of the obtained C/TiO_2 composite. In a previous in situ study on the conversion of anodic TiO_2/Ti_{poly} into TiO_xC_y/Ti_{poly} under UHV conditions, a substrate grain dependent chemical composition of the final TiO_xC_y film was found, evidencing that also under different synthesis conditions (temperature, pressure, and carbon source), effects of the polycrystalline substrate need to be taken into account.[20] A detailed investigation of the temperature-dependence of the surface chemistry and the structure of this system is ongoing and will be published separately.

From the FWHM values of the anatase E_g (143 cm^{-1}) bands it is deduced that the TiO_2^{ref} film consists of polycrystalline anatase with nanometer size crystallites. This may explain why

9228 | Phys. Chem. Chem. Phys., 2016, 18, 9220–9231

This journal is © the Owner Societies 2016

only nanocrystalline and no extended graphitic carbon layers are formed in the course of the thermal treatment. Furthermore, it gives an explanation for the inhomogeneous carbon coverage of TiO_2 on individual substrate grains as observed with SPEM and SEM, which is particularly emphasized on top of grains that are tilted by $\Phi \leq \sim 15°$: a polycrystalline TiO_2 film consists of anatase domains that have different orientations exposing different faces at the surface, which in turn affects their activity towards C_2H_2 decomposition. The reason for this is that different anatase faces exhibit different fractions of active $Ti^{4+}–O^{2-}$ centers. According to the literature a high fraction of these sites appears to be present on dehydroxylated, stoichiometric and extended (001) and/or (010) planes of crystalline anatase.[55,56]

Our results demonstrate that the peculiar properties of compact anodic TiO_2 films on Ti_{poly} have an important impact on the synthesis of $C/TiO_2/Ti_{poly}$ composites *via* the carbothermal route. The obtained substrate grain dependent chemical composition and structure of the film is likely to affect its overall performance when applied in electrocatalysis or Li-ion battery studies. For example, it is known that local variations in the charge transfer kinetics play a crucial role in the overall activity of electrocatalysts.[57] The grain dependent electrochemical stability of Pt/TiO_xC_y found in ref. 16 is another consequence of these properties of anodic TiO_2 on Ti_{poly}. An adapted design of C/TiO_2 films requires a detailed knowledge of the substrate texture and a controlled crystallization of the anodic film during the carbothermal treatment. The presence of crystalline anatase TiO_2 required for the reactive decomposition of C_2H_2 at 550 °C and atmospheric pressure has implications on the carbothermal synthesis of functional C/TiO_2 materials in general.

5. Conclusions

In the present work the substrate grain dependent properties of planar $C/TiO_2/Ti_{poly}$ composite films that are synthesized *via* carbothermal treatment of compact anodic TiO_2 with C_2H_2 in a flow reactor at 550 °C have been investigated. A pronounced correlation between the amount of deposited carbon and the Ti substrate grain orientations is observed: a significantly high amount of graphitic carbon is deposited on the anodic TiO_2 film on top of $\sim Ti(0001)$ grains than on TiO_2 on top of $\sim Ti\{hki0\}$ grains. The origin of the grain effect is identified as a substrate grain-dependent crystallization of the initially amorphous anodic TiO_2 film to nanocrystalline anatase during the thermal treatment, which in turn affects the activity of TiO_2 towards C_2H_2 decomposition to form nanocrystalline graphite. This effect emphasizes the importance of TiO_2 precursor crystallinity for the synthesis of C/TiO_2 functional materials *via* a carbothermal route. In the case of anodic TiO_2 films, the crystallization needs to be guided towards extended single crystalline anatase domains exposing their most active facets to enable the deposition of extended graphite layers, which, in combination with the possibility of nanostructuring anodic TiO_2, provides a highly interesting functional material. Indeed, nanotubular C/TiO_{2-x} composite layers, synthesized *via* the carbothermal route, have shown promising Li storage capacities,[15] which may be further improved by means of an optimized synthesis, taking into account the crystallization characteristics of anodic films.

A detailed knowledge of local physico-chemical properties, as-obtained in this study, is important to understand the overall performance of functional materials. In view of the potential applications of C/TiO_2 composite materials in energy conversion and storage, the herein introduced planar $C/TiO_2/Ti_{poly}$ composite is proposed as a model system for the investigation of property–performance relationships. Taking advantage of the substrate grain effect, two-dimensional property maps of the C/TiO_2 film that correlate (substrate grain dependent) intrinsic physico-chemical properties, such as chemical composition or morphology, and functional properties, such as electric conductivity, catalytic activity or (electro-)chemical stability, will give valuable information about the material. This can be realized by means of local analysis tools, such as SPEM[21] and micro-electrochemistry.[58]

Author contributions

The manuscript was written through contributions of all authors. CR planned and executed or coordinated the experiments, evaluated the data and drafted the manuscript. MF participated in the SPEM experiments and contributed to the SPEM data evaluation. CVV and LC participated in the SPEM experiments. NB evaluated the EBSD measurements which were performed by SJ. CH performed the Raman measurements. LG and MA gave technical support at the ESCAmicroscopy beamline of the Elettra Synchrotron in Trieste. SA conceived of the SPEM study and gave advice for the data evaluation. GG gave general advisory support. JKL supervised the study and actively participated in drafting the manuscript.

All authors have given approval to the final version of the manuscript.

Funding sources

Conflicts of interest

The authors declare no competing financial interest.

Abbreviations

UHV	Ultra-high vacuum
EBSD	Electron backscatter diffraction
AFM	Atomic force microscopy
SEM	Scanning electron microscopy
SPEM	Scanning photoelectron microscopy
FWHM	Full width at half maximum
NCG	Nanocrystalline graphite

This journal is © the Owner Societies 2016

Phys. Chem. Chem. Phys., 2016, **18**, 9220–9231 | 9229

Acknowledgements

References

1 L. Xiong and A. Manthiram, *Electrochim. Acta*, 2004, **49**, 4163.
2 J. Tian, G. Sun, M. Cai, Q. Mao and Q. Xin, *J. Electrochem. Soc.*, 2008, **155**, B187.
3 P. V. Kamat, *J. Phys. Chem. Lett.*, 2010, **1**, 520.
4 T. Fröschl, U. Hörmann, P. Kubiak, G. Kučerová, M. Pfanzelt, C. K. Weiss, R. J. Behm, N. Hüsing, U. Kaiser, K. Landfester and M. Wohlfahrt-Mehrens, *Chem. Soc. Rev.*, 2012, **41**, 5313.
5 M. Dahl, Y. Liu and Y. Yin, *Chem. Rev.*, 2014, **114**, 9853.
6 W. Fan, Q. Lai, Q. Zhang and Y. Wang, *J. Phys. Chem. C*, 2011, **115**, 10694.
7 B. Tryba, A. W. Morawski, T. Tsumura, M. Toyoda and M. Inagaki, *J. Photochem. Photobiol., A*, 2004, **167**, 127.
8 Y. Zhang, Z.-R. Tang, X. Fu and Y.-J. Xu, *ACS Nano*, 2010, **4**, 7303.
9 Y. T. Liang, B. K. Vijayan, O. Lyandres, K. A. Gray and M. C. Hersam, *J. Phys. Chem. Lett.*, 2012, **3**, 1760.
10 M. Favaro, S. Agnoli, C. Di Valentin, C. Mattevi, M. Cattelan, L. Artiglia, E. Magnano, F. Bondino, S. Nappini and G. Granozzi, *Carbon*, 2014, **68**, 319.
11 A. Zana, C. Rüdiger, J. Kunze-Liebhäuser, G. Granozzi, N. E. A. Reeler, T. Vosch, J. J. K. Kirkensgaard and M. Arenz, *Electrochim. Acta*, 2014, **139**, 21.
12 R. Hahn, F. Schmidt-Stein, J. Salonen, S. Thiemann, Y. Song, J. Kunze, V.-P. Lehto and P. Schmuki, *Angew. Chem., Int. Ed.*, 2009, **48**, 7236.
13 Y. Kado, R. Hahn and P. Schmuki, *J. Electroanal. Chem.*, 2011, **662**, 25.
14 C. Rüdiger, F. Maglia, S. Leonardi, M. Sachsenhauser, I. D. Sharp, O. Paschos and J. Kunze, *Electrochim. Acta*, 2012, **71**, 1.
15 J. Brumbarov, J. P. Vivek, S. Leonardi, C. Valero-Vidal, E. Portenkirchner and J. Kunze-Liebhäuser, *J. Mater. Chem. A*, 2015, **3**, 16469.
16 C. Rüdiger, J. Brumbarov, F. Wiesinger, S. Leonardi, O. Paschos, C. Valero Vidal and J. Kunze-Liebhäuser, *ChemCatChem*, 2013, **5**, 3219.
17 L. Calvillo, G. García, A. Paduano, O. Guillén-Villafuerte, C. Valero-Vidal, A. Vittadini, M. Bellini, A. Lavacchi, S. Agnoli, A. Martucci, J. Kunze-Liebhäuser, E. Pastor and G. Granozzi, *ACS Appl. Mater. Interfaces*, 2016, **8**, 716.
18 A. Aladjem, *J. Mater. Sci.*, 1973, **8**, 688.
19 P. Roy, S. Berger and P. Schmuki, *Angew. Chem., Int. Ed.*, 2011, **50**, 2904.
20 L. Calvillo, D. Fittipaldi, C. Rüdiger, S. Agnoli, M. Favaro, C. Valero-Vidal, C. Di Valentin, A. Vittadini, N. Bozzolo, S. Jacomet, L. Gregoratti, J. Kunze-Liebhäuser, G. Pacchioni and G. Granozzi, *J. Phys. Chem. C*, 2014, **118**, 22601.
21 M. K. Abyaneh, L. Gregoratti, M. Amati, M. Dalmiglio and M. Kiskinova, *e-J. Surf. Sci. Nanotechnol.*, 2011, **9**, 158.
22 L. Gregoratti, A. Barinov, E. Benfatto, G. Cautero, C. Fava, P. Lacovig, D. Lonza, M. Kiskinova, R. Tommasini, S. Mähl and W. Heichler, *Rev. Sci. Instrum.*, 2004, **75**, 64.
23 H.-J. Bunge, *Texture Analysis in Materials Science: Mathematical Methods*, Butterworths & Co, London, U.K., 2nd edn, 1982.
24 The lattice cell was drawn with the software Diamond 4.0 (demonstration version).
25 U. König and B. Davepon, *Electrochim. Acta*, 2001, **47**, 149.
26 M. V. Diamanti, M. P. Pedeferri and C. A. Schuh, *Metall. Mater. Trans. A*, 2008, **39**, 2143.
27 A. K. Sharma, *Thin Solid Films*, 1992, **208**, 48.
28 S. Kudelka and J. W. Schultze, *Electrochim. Acta*, 1997, **42**, 2817.
29 J. W. Schultze, B. Davepon, F. Karman, C. Rosenkranz, A. Schreiber and O. Voigt, *Corros. Eng., Sci. Technol.*, 2004, **39**, 45.
30 T. Ohsaka, F. Izumi and Y. Fujiki, *J. Raman Spectrosc.*, 1978, **7**, 321.
31 S. P. S. Porto, P. A. Fleury and T. C. Damen, *Phys. Rev.*, 1967, **154**, 522.
32 A. Mooradian and P. M. Raccah, *Phys. Rev. B: Solid State*, 1971, **3**, 4253.
33 S.-W. Hsu, T.-S. Yang, T.-K. Chen and M.-S. Wong, *Thin Solid Films*, 2007, **515**, 3521.
34 J. Zhang, M. Li, Z. Feng, J. Chen and C. Li, *J. Phys. Chem. B*, 2006, **110**, 927.
35 A. C. Ferrari and J. Robertson, *Phys. Rev. B: Condens. Matter Mater. Phys.*, 2000, **61**, 95.
36 M. Favaro, S. Leonardi, C. Valero-Vidal, S. Nappini, M. Hanzlik, S. Agnoli, J. Kunze-Liebhäuser and G. Granozzi, *Adv. Mater. Interfaces*, 2015, **2**, 1400462.
37 M. Fernández-García, X. Wang, C. Belver, J. C. Hanson and J. A. Rodriguez, *J. Phys. Chem. C*, 2007, **111**, 674.
38 V. Likodimos, T. Stergiopoulos, P. Falaras, J. Kunze and P. Schmuki, *J. Phys. Chem. C*, 2008, **112**, 12687.
39 F. D. Hardcastle, H. Ishihara, R. Sharma and A. S. Biris, *J. Mater. Chem.*, 2011, **21**, 6337.
40 H. Matsuura, M. Hiraishi and T. Miyazawa, *Spectrochim. Acta*, 1972, **2**, 2299.
41 J. F. Mammone and S. K. Sharma, *J. Phys. Chem.*, 1980, **84**, 3130.
42 N. Ito, T. Fujiyama and Y. Udagawa, *Bull. Chem. Soc. Jpn.*, 1983, **56**, 379.
43 I. H. Boyaci, H. E. Genis, B. Guven, U. Tamer and N. Alper, *J. Raman Spectrosc.*, 2012, **43**, 1171.
44 D. Bersani, P. P. Lottici and X.-Z. Ding, *Appl. Phys. Lett.*, 1998, **72**, 73.

9230 | *Phys. Chem. Chem. Phys.*, 2016, **18**, 9220–9231

This journal is © the Owner Societies 2016

45 W. F. Zhang, Y. L. He, M. S. Zhang, Z. Yin and Q. Chen, *J. Phys. D: Appl. Phys.*, 2000, **33**, 912.

46 A. Li Bassi, D. Cattaneo, V. Russo, C. E. Bottani, E. Barborini, T. Mazza, P. Piseri, P. Milani, F. O. Ernst, K. Wegner and S. E. Pratsinis, *J. Appl. Phys.*, 2005, **98**, 1.

47 T. Ohsaka, *J. Phys. Soc. Jpn.*, 1980, **48**, 1661.

48 D. Regonini, A. Jaroenworaluck, R. Stevens and C. R. Bowen, *Surf. Interface Anal.*, 2010, **42**, 139.

49 B. Davepon, J. W. Schultze, U. König and C. Rosenkranz, *Surf. Coat. Technol.*, 2003, **169–170**, 85.

50 S. Kudelka, A. Michaelis and J. W. Schultze, *Electrochim. Acta*, 1996, **41**, 863.

51 T. Tsumura, N. Kojitani, I. Izumi, N. Iwashita, M. Toyoda and M. Inagaki, *J. Mater. Chem.*, 2002, **12**, 1391.

52 M. Pfanzelt, P. Kubiak, U. Hörmann, U. Kaiser and M. Wohlfahrt-Mehrens, *Ionics*, 2009, **15**, 657.

53 I. Eswaramoorthi and L.-P. Hwang, *Diamond Relat. Mater.*, 2007, **16**, 1571.

54 S. M. Jain, J. J. Biedrzycki, V. Maurino, A. Zecchina, L. Mino and G. Spoto, *J. Mater. Chem. A*, 2014, **2**, 12247.

55 J. J. Biedrzycki, S. Livraghi, I. Corazzari, L. Mino, G. Spoto and E. Giamello, *Langmuir*, 2015, **31**, 569.

56 G. Martra, *Appl. Catal., A*, 2000, **200**, 275.

57 A. N. Patel, M. G. Collignon, M. A. O'Connell, W. O. Y. Hung, K. McKelvey, J. V. MacPherson and P. R. Unwin, *J. Am. Chem. Soc.*, 2012, **134**, 20117.

58 S. O. Klemm, J.-C. Schauer, B. Schuhmacher and A. W. Hassel, *Electrochim. Acta*, 2011, **56**, 4315.

This journal is © the Owner Societies 2016

Phys. Chem. Chem. Phys., 2016, **18**, 9220–9231 | 9231